Shallow waters resistance of an accelerating ship

Y H Liu[1], **M Terziev**[1]

[1]Department of Naval Architecture, Ocean and Marine Engineering, Henry Dyer Building, University of Strathclyde, 100 Montrose Street, Glasgow, UK.

yihan.liu.100@strath.ac.uk

momchil.terziev@strath.ac.uk

Abstract. This paper investigates the acceleration resistance of a vessel in shallow waters using potential flow and CFD methods. Results indicated a pronounced resistance peak near the critical depth Froude number. The peak's location and magnitude were sensitive to acceleration intensity and water depth. Excellent agreement between potential flow and CFD methods was found in low and high depth Froude number ranges, suggesting their effectiveness and cost-efficiency. However, non-linear effects affected the resistance peak's magnitude and position, leading to slight disagreements between the methods. The solvers' variation was observed to be sensitive to the investigated parameters.

1. Introduction

Ship resistance prediction has traditionally focused on steady conditions, determining a single resistance value for each combination of speed and water depth. However, recent research has shed light on the unsteady nature of ship resistance. Studies by Havelock [1], Lunde [2][3], and [4] have explored transient wave resistance, considering the effects of acceleration and proposing mathematical theories. Calisal [5] extended these theories to incorporate wave pattern development in unrestricted water. Furthermore, Day et al. [6] investigated the influence of finite depth and width effects in a towing tank.

The investigation of unsteady resistance has been motivated by the performance considerations of unconventional vessels, such as hovercraft [7][10]. In these studies, the vessels are often simplified as two-dimensional pressure distributions on the water surface [11][12]. Researchers have observed oscillations in the time-history signal of towed craft, presenting challenges in accurately measuring steady resistance values [13]. While various theories on unsteady wave drag have been proposed, there has been limited exploration of the scenario involving a ship accelerating past a critical depth Froude number.

In the field of aerodynamics, exceeding the speed of sound results in the occurrence of a sonic boom. Similarly, phenomena analogous to a sonic boom have been observed when a vessel encounters variations in water depth [4]. A change in water depth can cause the wave speed to decrease below the vessel's speed, leading to the generation of significant amplitude waves [4]. As the vessel passes over this change, the depth Froude number undergoes a transition from a subcritical value (F_h <1) to a supercritical value (F_h >1). Unlike in aerodynamics, where trans-critical phenomena are primarily observed through changes in speed, hydrodynamics allows for manipulation of water depth and/or vessel speed to achieve similar effects.

2. Methodology

In this study, the potential flow solver MHydro [20] is employed, which utilizes a 3D boundary element method (BEM) based on a Rankine type Green function. This solver is specifically chosen to investigate unsteady free surface effects. MHydro has been successfully utilized in previous research on ship hydrodynamics in both deep and shallow water by Yuan et al. [21].

To obtain the solution, it is crucial to establish correlations between all results at each time step, allowing for the preservation of unsteady terms in the free-surface boundary conditions. This capability enables the simulation of unsteady effects on the free surface. The methodology employed in this study will be described in detail in the subsequent sections.

2.1. Description of the problem

The problem is described using two right-handed coordinate systems, as illustrated in Figure 1. The first coordinate system, denoted as *O-XYZ*, is fixed to the Earth. The second coordinate system, denoted as o_0-$x_0y_0z_0$, is fixed to the ship hull and moves along with the ship. In both coordinate systems, the positive x-axis points towards the bow of the ship, the positive y-axis points towards the port side of the ship, and the positive z-axis points upward. The undisturbed calm free surface is situated at z=0.

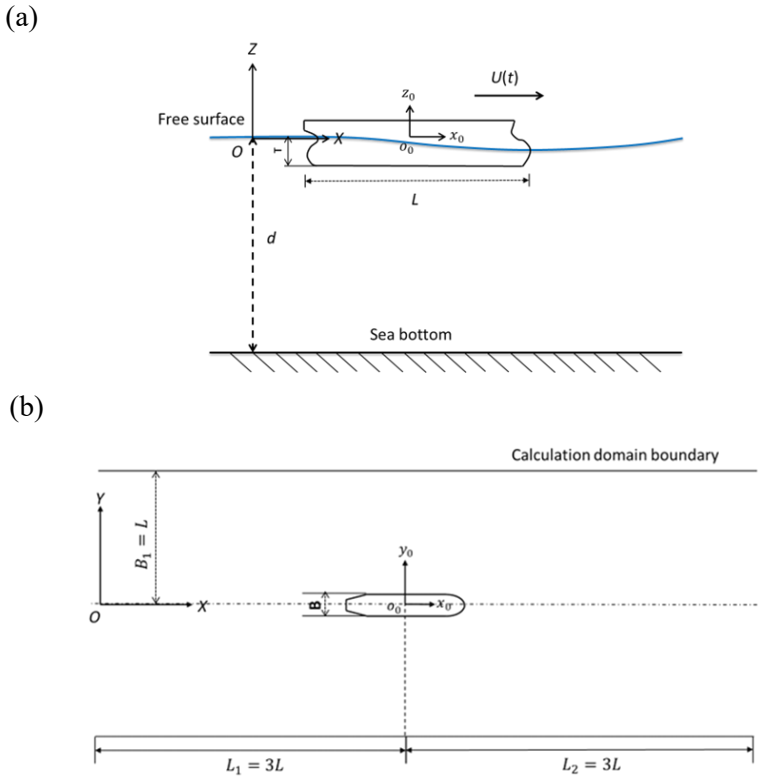

Figure 1. Sketch of the problem. In (a), L is the length of the ship and $U(t)$ is the ship velocity which is changing with time. T represents the draft of the ship while the water depth is denoted as d. (b) shows a top view of the problem, where it can be seen that the distance between the front and rear boundaries of the computational domain and the midship point are both $3L$. On the other hand, both the port and starboard boundaries are L away from the centreline of the ship. Finally, B in this figure represents the ship breadth.

2.2. Boundary value problem

There are only two boundary conditions in this problem: the body-surface condition and the free-surface condition. The body-surface condition is that the surface is impenetrable and the normal velocity of all cells on the body is equal to the speed U of the ship:

$$\frac{\partial \varphi}{\partial \boldsymbol{n}} = U n_1 \tag{1}$$

where $n = (n_1, n_2, n_3)$ is the unit normal vector on body-surface.

The free-surface condition in this method can be separated into two components: the dynamic free-surface condition and the kinematic free-surface condition. Since the method utilized in this study is based on potential flow, the fluid is assumed to be ideal, which implies that it is inviscid, irrotational, and incompressible. As a result, the free-surface conditions can be expressed using the velocity potential $\varphi(x, y, z, t)$ and the wave elevation $\zeta(x, y, t)$ as follows:

$$\varphi_t - U\varphi_x + g\zeta + \frac{1}{2}\left({\varphi_x}^2 + {\varphi_y}^2 + {\varphi_z}^2\right) + \frac{P}{\rho} = 0, on\ z = \zeta \tag{2}$$

$$\zeta_t - U\zeta_x + \varphi_x\zeta_x + \varphi_y\zeta_y - \varphi_z = 0, \qquad on\ z = \zeta \tag{3}$$

where g is the gravitational acceleration, ρ is the fluid density and P is the pressure on free surface, and $\varphi_t$and ζ_t are the respective time derivatives. Similarly, φ_x, φ_y and φ_z are directional derivatives.

To simplify the solution process, the nonlinear terms are disregarded while retaining the unsteady terms, as discussed earlier. Consequently, the simplified linear unsteady free-surface condition can be expressed as follows:

$$\varphi_t - U\varphi_x + g\zeta + \frac{1}{2}\left({\varphi_x}^2 + {\varphi_y}^2 + {\varphi_z}^2\right) = 0, on\ z = \zeta \tag{4}$$

$$\zeta_t - U\zeta_x - \varphi_z = 0, \qquad on\ z = \zeta \tag{5}$$

With the boundary conditions established, the subsequent step involves solving the resulting equations. To accomplish this, a three-level scheme is employed to discretize the free surface conditions:

$$(\varphi_t)_{i,j}^{m+1} = \frac{1}{\Delta t}\left(\frac{3}{2}\varphi_{i,j}^{m+1} - 2\varphi_{i,j}^{m} + \frac{1}{2}\varphi_{i,j}^{m-1}\right) \tag{6}$$

$$(\zeta_t)_{i,j}^{m+1} = \frac{1}{\Delta t}\left(\frac{3}{2}\zeta_{i,j}^{m+1} - 2\zeta_{i,j}^{m} + \frac{1}{2}\zeta_{i,j}^{m-1}\right) \tag{7}$$

where m represents the mth time step, i and j indicate location of the cell on the free surface. Substituting the Eq. (6) and Eq. (7) into the kinetic free-surface condition, allows one to obtain the value of $(\zeta)_{i,j}^{m+1}$:

$$\frac{1}{\Delta t}\left(\frac{3}{2}\zeta_{i,j}^{m+1} - 2\zeta_{i,j}^{m} + \frac{1}{2}\zeta_{i,j}^{m-1}\right) - U\frac{1}{\Delta x}\left(\frac{3}{2}\zeta_{i,j}^{m+1} - 2\zeta_{i,j+1}^{m+1} + \frac{1}{2}\zeta_{i,j+2}^{m+1}\right) - \frac{\partial \varphi_{i,j}^{m+1}}{\partial z} = 0 \tag{8a}$$

$$\left(\frac{1}{\Delta t} - \frac{3}{2}\frac{U}{\Delta x}\right)\zeta_{i,j}^{m+1} + 2\frac{U}{\Delta x}\zeta_{i,j+1}^{m+1} - \frac{1}{2}\frac{U}{\Delta x}\zeta_{i,j+2}^{m+1} = \frac{2}{\Delta t}\zeta_{i,j}^{m} - \frac{1}{2}\frac{1}{\Delta t}\zeta_{i,j}^{m-1} + \frac{\partial \varphi_{i,j}^{m+1}}{\partial z} \tag{8b}$$

Then, all variables in the dynamic free-surface condition can be updated with the results obtained:

$$\frac{1}{\Delta t}\left(\frac{3}{2}\varphi_{i,j}^{m+1} - 2\varphi_{i,j}^{m} + \frac{1}{2}\varphi_{i,j}^{m-1}\right) - U\frac{\partial \varphi_{i,j}^{m+1}}{\partial x} + g\zeta_{i,j}^{m+1} = 0 \tag{9a}$$

$$\frac{3}{2}\frac{1}{\Delta t}\varphi_{i,j}^{m+1} - U\frac{\partial \varphi_{i,j}^{m+1}}{\partial x} = \frac{2}{\Delta t}\varphi_{i,j}^{m} - \frac{1}{2}\frac{1}{\Delta t}\varphi_{i,j}^{m-1} - g\zeta_{i,j}^{m+1} \tag{9b}$$

In the above process, as the number of iterations k increases, all variables will be continuously updated until both $\left|\varphi_{i,j}^{m+1,k} - \varphi_{i,j}^{m+1,k-1}\right| < \varepsilon$ and $\left|\zeta_{i,j}^{m+1,k} - \zeta_{i,j}^{m+1,k-1}\right| < \varepsilon$ are satisfied.

In order to solve the above-mentioned boundary value problem, we developed a programme, namely MHydro, based on the Rankine source panel method. Once the potential is obtained, it is possible to calculate the pressure distribution and the forces/moments acting on the hull using Bernoulli's equation, which can be expressed as follows:

$$P = -\rho\left[\varphi_t - U\varphi_x + \frac{1}{2}\left(\varphi_x^2 + \varphi_y^2 + \varphi_z^2\right)\right] \tag{10}$$

$$F_i = \iint_S P n_i ds, i = 1, 2, \dots, 6 \tag{11}$$

where i represents the degree of freedom, and:

$$n_i = \begin{cases} \boldsymbol{n}, & i = 1, 2, 3 \\ \boldsymbol{x} \times \boldsymbol{n}, & i = 4, 5, 6 \end{cases} \tag{12}$$

3. Case study selection

For the case studies in this research, the Wigley hull has been selected, and its specifications are provided in Table 1. Although there are several experimental results available for the Wigley hull, there is currently no data specifically replicating the trans-critical behaviour of an accelerating ship. By choosing the Wigley hull, we aim to maximize the potential for other researchers to utilize the results presented here in their future studies. This is due to the hull's ease of mathematical modelling and its common usage in potential flow-based investigations [13], [22]-[24].

Table 1. Wigley hull principal dimensions.

Parameter	Symbol	Value	Units
Length	L	3	m
Draft	T	0.1875	m
Beam	B	0.3	m

The depth Froude number serves as the basis for varying the parameters in the test matrix, namely the ship speed U and the water depth d. Following the approach of Day et al. [6] and Li et al. [13], multiples of the gravitational acceleration g are utilized to modify the ship speed. Previous studies focused on rapidly accelerating the hull to a target speed and maintaining that speed, using values ranging from $0.08g$ to $0.02g$. However, the objective of the current study is to observe transient phenomena during acceleration. Therefore, the maximum acceleration intensity chosen for this study is $0.02g$, which corresponds to the lowest acceleration intensity used by Day et al. [6] and Li et al. [13]. Additionally, acceleration intensities of $0.01g$, $0.005g$, and $0.002g$ are also employed.

To assess the impact of water depth, the test matrix in Table 2 combines acceleration intensities with d/T ratios of 1.2 and 1.5. The cases progress up to a maximum water depth Froude number of 2. In the CFD simulations, steady and constant velocity cases are used to estimate the deviation in resistance between fixed speed and accelerating conditions. Table 3 provides the water depth Froude numbers corresponding to different water depths for constant velocities.

Table 2. Case studies modelling the acceleration resistance of the Wigley hull.

Case number	Acceleration	d/T
1	$0.02g$	1.2
2	$0.01g$	
3	$0.005g$	
4	$0.002g$	
5	$0.02g$	1.5
6	$0.01g$	
7	$0.005g$	
8	$0.002g$	

Table 3. Constant velocity cases modelled using CFD.

Case number	Depth Froude number	*d*/*T*
9	0.60	
10	0.80	
11	0.89	
12	0.95	
13	1.00	1.2
14	1.05	
15	1.20	
16	1.40	
17	1.70	
18	0.60	
19	0.80	
20	0.89	
21	0.95	
22	1.00	1.5
23	1.05	
24	1.20	
25	1.40	
26	1.70	

4. Results and discussion

The potential flow theory provides results for wave-making resistance, whereas the CFD solution yields three sets of resistance results: total resistance (R_T), frictional resistance (R_F), and pressure resistance (R_P). The pressure resistance is further divided into normal and tangential components, with R_F encompassing the effects of surface curvature. On the other hand, R_P represents a combination of viscous pressure resistance and wave resistance [25]. However, the viscous pressure resistance typically constitutes a small portion of the total resistance across all speeds [26]. Since wave resistance predominates over pressure resistance, it is possible to compare the results without the need to separate the pressure resistance into its individual components.

4.1. Pressure and wave resistance

This section compares the wave and pressure resistance values obtained as the ship accelerates for the two modeled depth-to-draft ratios. Figure 2 illustrates the comparison between the CFD method and MHydro for all cases listed in the test matrix (Table 2), including the constant velocity cases modeled using CFD (Table 3). All forces are made dimensionless using the ship mass force F_m, as described in [6]. A pronounced peak can be observed in all cases near F_h =1. In the steady problem (i.e., constant speed with no acceleration), such a peak is generated by the mutual interference of the fore and aft wave systems produced by the ship. The resistance curves in Figure 2 indicate that this type of interference reaches its maximum between F_h =1.05 and F_h =1.2, depending on the value of the dimensionless acceleration (a/g).

It should be noted that the peak values shown in Figure 2 for the constant speed case are based on a limited number of selected points, and they may not precisely indicate the exact peak value. The curve only provides an approximate range within which the peak value is expected to appear. However, it is evident that the increase in resistance is significantly influenced by the water depth, as demonstrated by the higher F_x values when d/T =1.2 compared to d/T =1.5. This phenomenon undergoes changes

when acceleration is introduced. In other words, the presence of acceleration generates an unsteady wave that has a notable impact on the resistance.

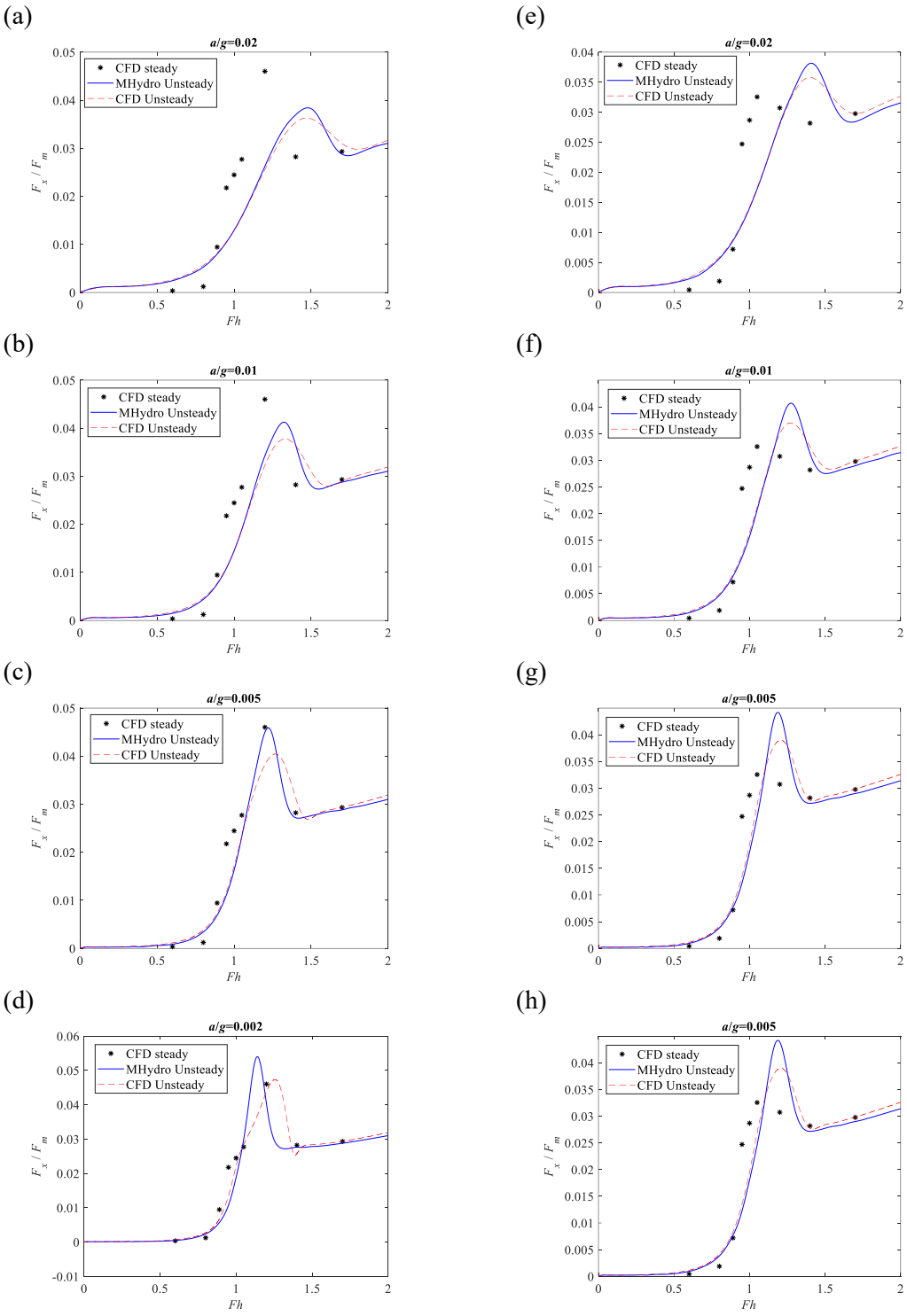

Figure 2. Changes of resistance during ship acceleration. The tiles on the left show d/T =1.2 while the tiles on the right show d/T =1.5. F_x is the wave resistance obtained by MHydro and pressure resistance obtained through the URANS method described previously. It also should be noted that the results of CFD here are pressure resistance while MHydro results are only wave making resistance.

In terms of the discrepancy in the position of the two peaks, both solvers provide remarkably similar results for high accelerations. Interestingly, the difference between the predictions increases monotonically from 0.75% and 0.68% to 10.13% and 5.54% for d/T =1.2 and d/T =1.5, respectively. Further investigations are necessary to understand why the two sets of predictions performed better for the lowest acceleration when the water depth is slightly larger. This effect could potentially be attributed to the presence of nonlinear effects, which are known to become more significant with decreasing water depth. However, drawing definitive conclusions would require more detailed investigations, preferably incorporating experimental data to eliminate any bias in numerical or potential solutions.

When comparing the results obtained from MHydro and CFD, it can be observed that regardless of whether d/T =1.2 or d/T =1.5, the peak in the MHydro results occurs earlier than the peak predicted by CFD, and the resistance value obtained from MHydro is consistently higher. This difference becomes particularly pronounced when the acceleration is small. One possible explanation for this disparity is the inclusion of viscous and nonlinear terms in CFD. MHydro, on the other hand, provides a linear and unsteady result by neglecting nonlinear terms.

As the acceleration increases, the relative importance of the unsteady effect grows, overshadowing the nonlinear effects. Consequently, the unsteady effect becomes dominant when the acceleration is sufficiently large, which explains why there is less agreement between the results obtained from MHydro and CFD when the acceleration is small. Conversely, the difference between the results obtained from the two prediction methods is smallest when the acceleration is large. This discussion aligns with observations made in other studies concerning linear potential flow solutions near the critical depth Froude number [18], 0, [28].

4.2. Acceleration effects

As mentioned earlier, two key factors influencing the problem under investigation are the magnitude of acceleration and the water depth. This paper will discuss each of these factors in detail. Upon introducing acceleration, Figure 3 demonstrates that both the peak resistance value and its corresponding position undergo changes. Considering the satisfactory agreement between CFD and MHydro, additional case studies are explored in Figure 3 using only the potential flow solver. This choice is made due to its faster turnaround time and lower computational requirements.

Figure 3 illustrates that as the acceleration increases, the resistance peak becomes smaller and shifts towards higher values of the examined depth Froude number. This indicates that the unsteady effect generated by the acceleration significantly influences the results. The shifting position of the resistance peak can be attributed to the shock wave formed at the bow due to the acceleration. During the initial stages when the ship speed is low, a shock wave is emitted forward, resulting in additional wave/pressure resistance. As the ship speed matches the speed of the wave, the wave-making resistance reaches its maximum, which is depicted as the peak in Figure 2.

In simpler terms, as the acceleration increases, the velocity of the shock wave generated by the ship also increases. This means that the ship needs to reach a higher speed to catch up with the shock wave. Consequently, the position of the resistance peak is delayed at higher accelerations. As the ship continues to accelerate, it eventually overtakes the shock wave, resulting in a sharp drop in resistance for a narrow range of F_h values, followed by a linear increase.

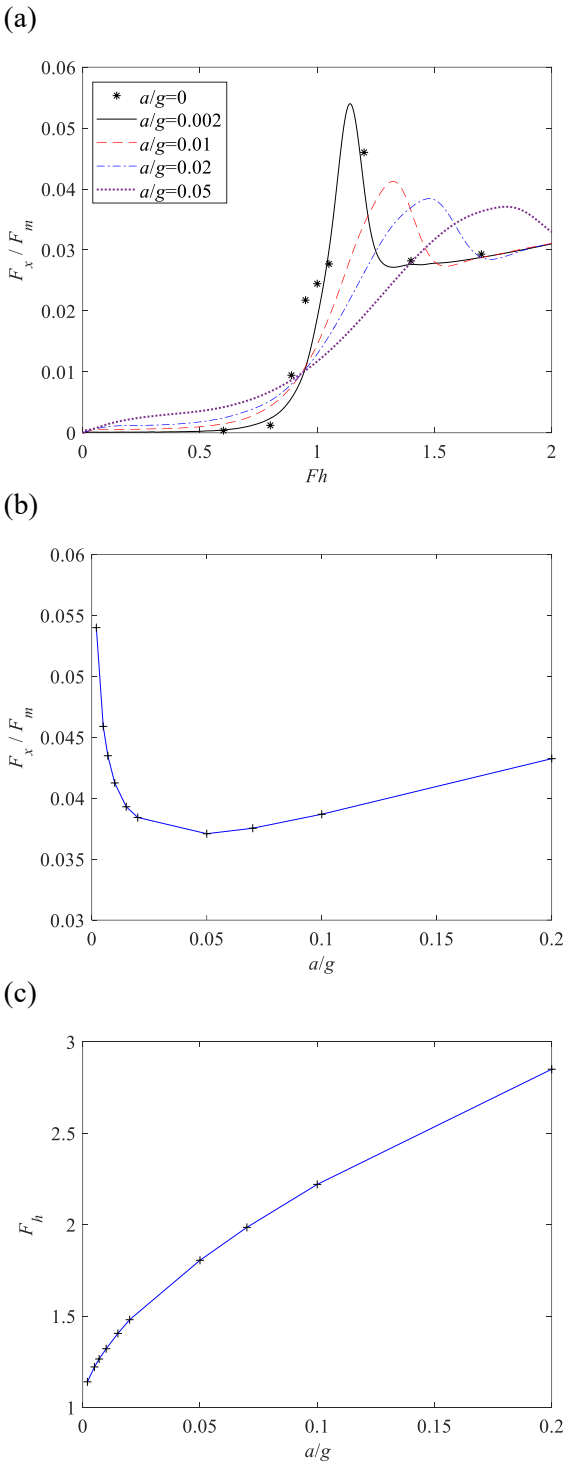

Figure 3. (a) Changes of fully unsteady resistance with varying acceleration; (b) Resistance peak value for different accelerations; (c) Peak location at different acceleration; Cases depicted correspond to d/T =1.2.

Another notable observation from the presented results is that irrespective of the acceleration, the time-history of resistance converges to a single point near F_h =1. Beyond this point, the resistance exhibits approximately linear growth until it reaches the resistance peak. Figure 4 (a) and Figure 4 (b) illustrate these findings for d/T =1.2 and d/T =1.5, respectively.

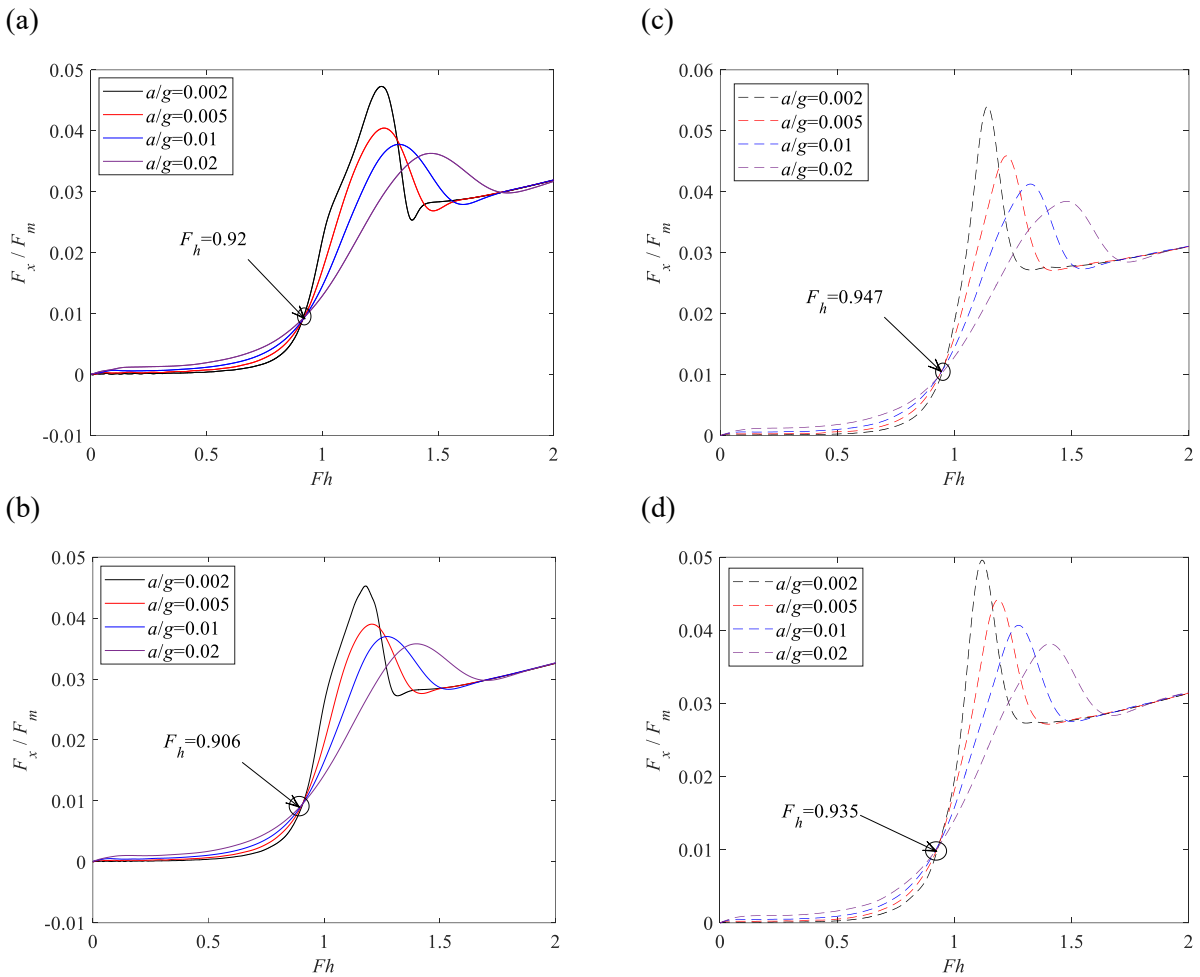

Figure 4. Resistance time-history for all acceleration intensities while solid lines show the results obtained using CFD and dashed lines show the results obtained using MHydro. (a) Resistance time-history at d/T =1.2 for CFD; (b) Resistance time-history at d/T =1.5 for CFD; (c) Resistance time-history at d/T =1.2 for MHydro; (d) Resistance time-history at d/T =1.5 for MHydro.

For the water depth corresponding to d/T =1.5, the CFD results indicate that the resistance time-histories coincide at approximately F_h =0.906, whereas the potential flow results predict this point at approximately F_h =0.935. Similarly, for d/T =1.2, CFD predicts a shift in this point to approximately F_h =0.92, while MHydro places it at approximately F_h =0.947. Before and after the point of intersection in the resistance time-histories, the resistance follows distinct paths. To the best of the authors' knowledge, such phenomena have not been documented in the existing literature.

To investigate the cause of this phenomenon, Figure 5 presents wave fields at different accelerations near the intersection point. As F_h or the acceleration varies, wave elevations at the bow and stern also change correspondingly. The wave at the bow is primarily influenced by the ship's velocity, which is relatively straightforward to comprehend. However, the situation is different for waves at the stern.

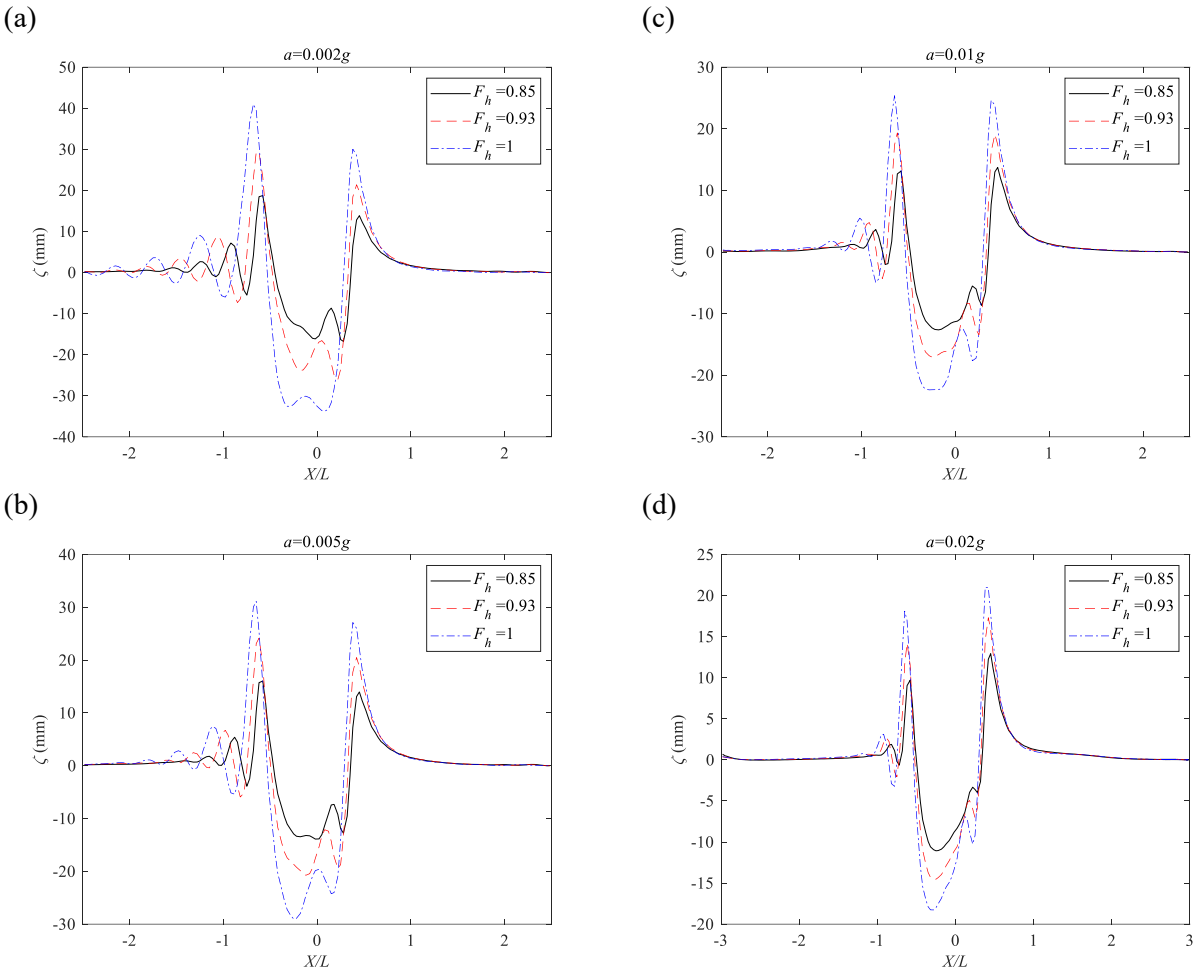

Figure 5. Wave elevations on the port side of ship with different accelerations (y/L=0.0167). These results were computed using MHydro for d/T=1.2.

Figure 6 (a) illustrates that the wave elevation at the ship stern is inversely proportional to the acceleration. A higher acceleration leads to more pronounced unsteady effects, which, when combined with the original wave field at the ship stern, result in smaller wave peaks and troughs. Additionally, it should be noted that waves at the ship stern exhibit peaks before the critical speed and troughs after it. This indicates that when F_h <1, a smaller acceleration brings the wave elevation at the bow and stern closer together, resulting in lower wave resistance. However, after this point, as the acceleration decreases, the wave trough at the stern significantly increases. According to Bernoulli's equation, this leads to a decrease in the pressure field at the stern of the ship, resulting in greater wave resistance. This explains the observed intersection of wave resistance in Figure 4 and why the peak resistance value decreases with an increase in acceleration.

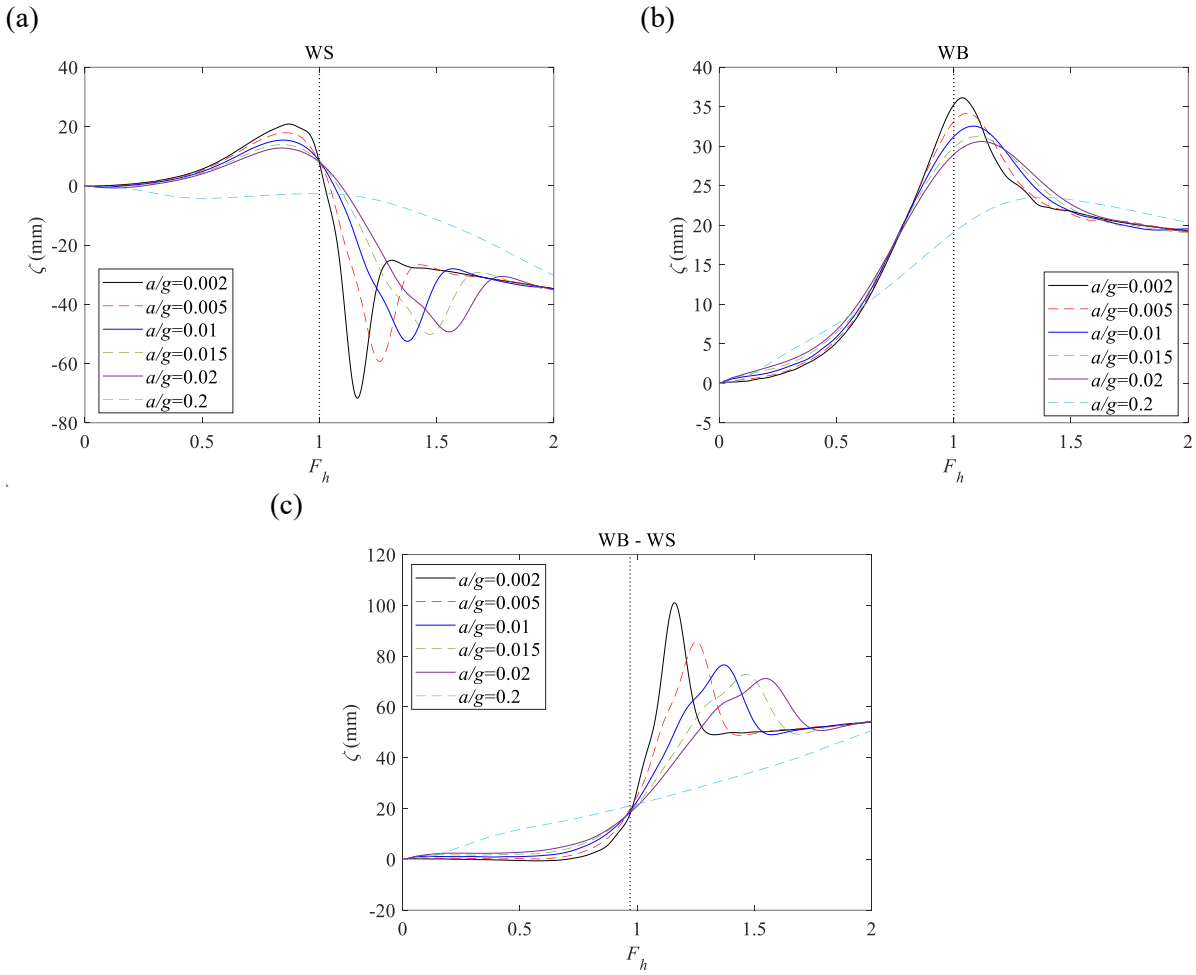

Figure 6. Wave elevations around the ship stern and bow with different accelerations. (a) Stern wave (WS); (b) Bow wave (WB); (c) Wave difference between ship bow and stern. These results were computed using MHydro for d/T =1.2.

4.3. Finite depth effects

The agreement between the constant speed and accelerating results depicted in Figure 2 (d) demonstrates that the effect of acceleration at a =0.002g and d/T =1.2 is minimal. However, there is a significant disparity between the corresponding values at d/T=1.5. This observation, combined with the shifting of the resistance peak along the F_h range due to varying acceleration, suggests that the water depth Froude number may not be the most suitable parameter to represent the time-varying velocity accurately.

Figure 7 shows a series of example cases computed with MHydro, with a fixed acceleration of a/g =0.02 for different depth-to-draft ratios (d/T =1.2-4). Within this framework, larger depth-to-draft ratios shift the resistance peak towards higher F_h values and diminish its magnitude. This effect is particularly noticeable between d/T =2 and d/T =4. The resistance penalty resulting from the shallow water effect at higher F_h values diminishes rapidly with increasing water depth. If the water depth were to exceed d/T =4, the distinctive resistance peak observed in shallow waters would disappear.

Another observation from Figure 7 is that shallow water conditions may provide an advantage in terms of reduced resistance when accelerating a vessel. Specifically, the values illustrated for F_h =1 in Figure 7 (d) indicate that higher water depths correspond to higher resistance. For the given acceleration, the increase in resistance between very shallow water (d/T =1.2) and moderately shallow

water (d/T =4) exceeds 100%. This increase is a result of the delay in the occurrence of the resistance peak to higher depth Froude numbers, as shown in Figure 7 (c).

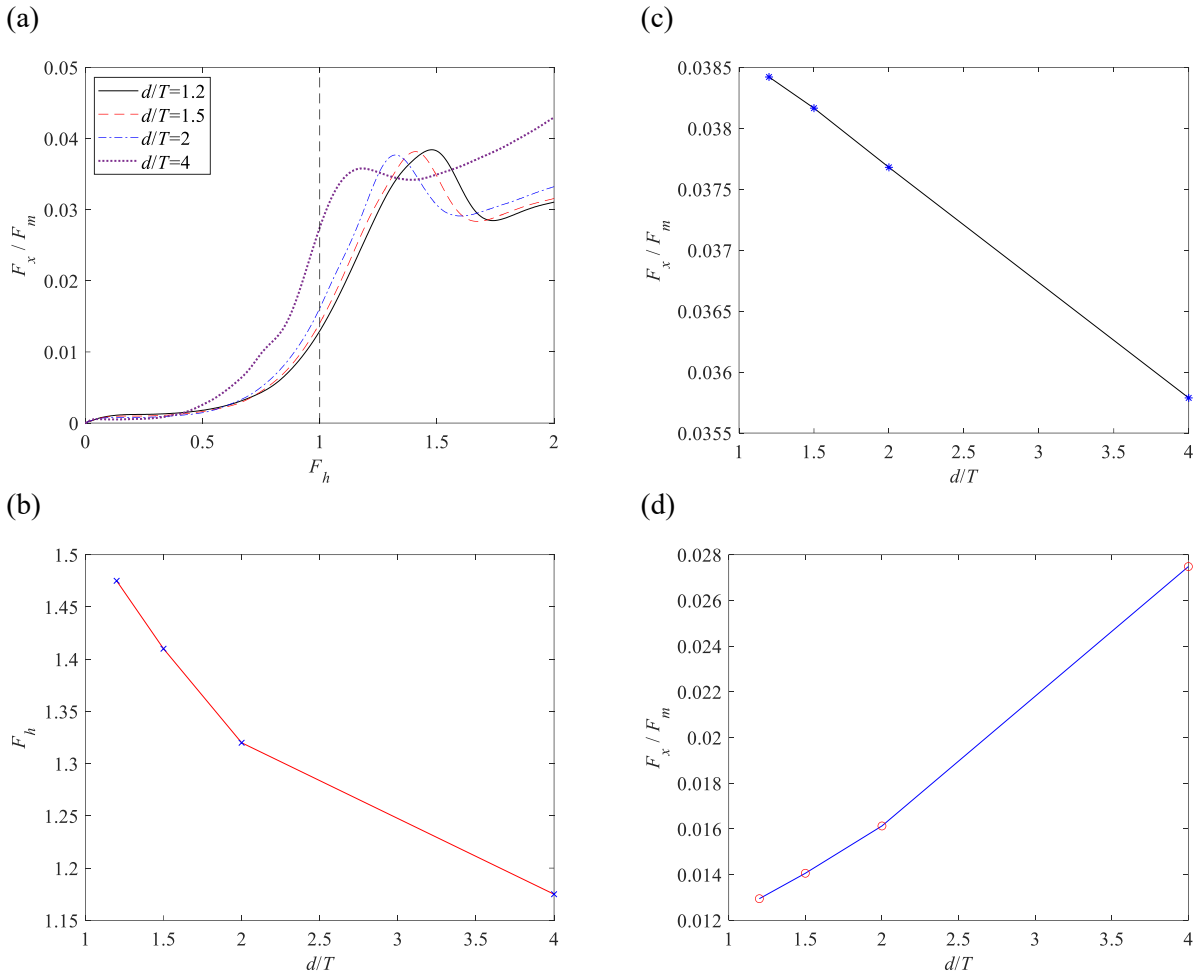

Figure 7. Wave resistance and associated peaks at different water depths, computed using MHydro. (a) shows the time-history of the resistance, (b) shows the magnitude of the peak for varying d/T ratios, (c) show the position of the peak as a function of d/T while (d) shows the resistance value at F_h=1.

4.4. Unsteady free surface effects

The results presented in the preceding sections, obtained through the solution of the fully unsteady boundary value problem (BVP) defined in Eq. (1), (4), and (5), provide valuable insights. To further investigate the effect of unsteadiness on the free surface boundary condition, a quasi-steady solution is proposed. In this approach, the time-dependent terms in Eq. (4) and (5) are ignored at each time step, while the body surface boundary condition in Eq. (1) remains unchanged. For both the steady and quasi-steady methods, the unsteady Bernoulli's equation in Eq. (12) is utilized to calculate the hydrodynamic force, specifically the wave-making resistance in the present study.

Figure 8 provides a direct comparison between the results obtained from the quasi-steady and unsteady free-surface solutions mentioned earlier. The observed discrepancies highlight the significance of considering the unsteady free-surface condition in the context of the acceleration problem investigated. Notably, the free-surface effects exert a predominant influence in the vicinity of

the critical speed region. Given the unsteady nature of the acceleration problem, it is crucial to take into account the unsteady terms in the free-surface condition.

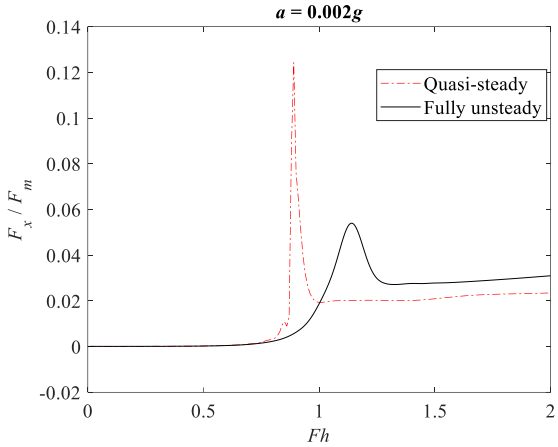

Figure 8 Wave-making resistance obtained by MHydro with and without considering the time-dependent terms on free-surface boundary condition. The water depth used here is d/T=1.2.

5. Conclusions and recommendations for future work

When a watercraft accelerates beyond the speed of the fundamental wave in a given medium, it experiences fluctuations in resistance. While such effects are well-known in aerodynamics, they had not been previously documented in the field of marine hydrodynamics, to the best of the authors' knowledge. In shallow water, the wave speed remains constant and depends only on gravitational acceleration and water depth. This provides an opportunity to investigate hydrodynamic equivalents to the sonic boom. The aim of the present study was to fill this gap in the literature by combining URANS and potential flow solutions.

The research focused on modelling four acceleration intensities and two water depths using the Wigley parabolic hull. In all cases, a pronounced resistance peak was observed near the critical depth Froude number. The results showed a maximum disagreement in predicting the location of the resistance peak along the examined depth Froude number, ranging from 5.54% to 12.44% for d/T=1.2 and 6.23% to 11.75% for d/T=1.5.

The findings indicated excellent agreement in the low and high-speed range beyond the critical transition, suggesting that resistance in that range is linear and primarily influenced by unsteady rather than nonlinear terms. Some deviations were observed between the two solvers near the critical speed, suggesting that nonlinear effects influence the solution in that range. An intersection point was identified near, but less than, F_h=1 for both modelled water depths, where all acceleration intensities intersect. This point's existence was attributed to the proximity of the trans-critical boundary and the fact that no steady flow is possible when the depth Froude number is unity.

While the results presented in this study demonstrate good agreement between the two solvers, it is important to note that experimental data on trans-critically accelerating ship resistance would be invaluable for validating the accuracy of the predictions. Furthermore, models of trans-critical acceleration in fully confined water are of particular interest, as the blockage ratio would also play a significant role. Such cases are intriguing because the trans-critical range can occupy a substantial portion of the depth Froude number, depending on the blockage [29].

References

[1] HAVELOCK TH 1949 The resistance of a submerged cylinder in accelerated motion *The Q. J. Mech. Appl. Mathematics* **2** 419–427

[2] Lunde J K 1957 The linearized theory of wave resistance and its application to ship shaped bodies in motion on the surface of a deep, previously undisturbed fluid (Technical University of Trondheim)

[3] Lunde J K 1951 On the linearized theory of wave resistance for deplacement ships in steady and accelerated motion (Technical University of Trondheim) pp 25-85

[4] Wehauden, J V 1961 *Effect of the initial acceleration upon the wave resistance of ship models* (Berkeley: California Univeristy Berkeley)

[5] Calisal S 1977 Effect of initial acceleration on ship wave pattern and wake survey methods *J. Ship Res.* **21** 239-247

[6] Day A H, Clelland D and Doctors L J 2009 Unsteady finite-depth effects during resistance tests on a ship model in a towing tank *J. of Mar. Sci. Technol.* **14** 387-397

[7] Doctors L J and Sharma S D 1972 The wave resistance of an air-cushion vehicle in steady and accelerated motion *J. Ship Res.* **16** 248-260

[8] Yeung R W 1975 Surface waves due to a maneuvering air-cushion vehicle *J. Ship Res.* **19** 224-242

[9] Haussling H J and Van Eseltine R T 1978 Waves and wave resistance for air-cushion vehicles with time-dependent cushion pressures *J. Ship Res.* **22** 170-177

[10] Barratt M J 1965 The wave drag of a hovercraft *J. Fluid Mech.* **22** 39-47

[11] Doctors L J 1975 The experimental wave resistance of an accelerating two-dimensional pressure distribution *J. Fluid Mech.* **72** 513-527

[12] Doctors L J 1993 On the use of pressure distributions to model the hydrodynamics of air-cushion vehicles and surface-effect ships *Naval Eng. J.* **105** 69-89

[13] Li M X, Yuan Z M and Yeung R W 2020 *Int. Conf. on Offshore Mechanics and Arctic Engineering* Vol 84379 (American)

[14] Jiang T, Henn R and Sharma S D 2002 *24th Symposium on Naval Hydrodynamics* (Japan: Fukuoka) pp 441-457

[15] Grue J 2017 Ship generated mini-tsunamis *J. Fluid Mech.* **816** 142-166

[16] Tuck E O 1966 Shallow-water flows past slender bodies *J. Fluid Mech.* **26** 81-95

[17] EO T 1967 Sinkage and trim in shallow water of finite width *Schiffstechnik* **14** 92-94

[18] Lea G K and Feldman J P 1972 Transcritical flow past slender ships *9th Symposium on Naval Hydrodynamics* (France: Paris) pp 1527–1542

[19] Gourlay T P and Tuck E O 2001 The maximum sinkage of a ship *J. Ship Res.* **45** 50-58

[20] Yuan Z M 2019 Ship hydrodynamics in confined waterways *J. Ship Res.* **63** 16-29

[21] Yuan Z M, Li L and Yeung R W 2019 Free-surface effects on interaction of multiple ships moving at different speeds *J. Ship Res.* **63** 251-267

[22] Yuan Z M, Incecik A and Jia L B 2014 A new radiation condition for ships travelling with very low forward speed *Ocean Eng.* **88** 298-309

[23] Andrun M, Blagojević B and Bašić J 2019 The influence of numerical parameters in the finite-volume method on the Wigley hull resistance *J. Eng. Marit. Environ.* **233** 1123-1132

[24] Bašić J, Blagojević B and Andrun M 2020 Improved estimation of ship wave-making resistance *Ocean Eng.* **200** 107079

[25] Molland A, Turnock S and Hudson D 2017 *Components of Hull Resistance In Ship Resistance and Propulsion: Practical Estimation of Ship Propulsive Power* (Cambridge: Cambridge University Press) pp 12-69

[26] Terziev M, Tezdogan T, Demirel Y K, Villa D, Mizzi S and Incecik A 2021 Exploring the effects of speed and scale on a ship's form factor using CFD *Int. J. Naval Architecture Ocean Eng.* **13** 147-162

[27] Tuck E O 1978 Hydrodynamic problems of ships in restricted waters *Annu. Rev. Fluid Mech.* **10** 33-46
[28] Tuck E O 1970 Shallow wave problems in ship hydrodynamics *8th Symposium Naval Hydrodynamics* (Pasadena)
[29] Lataire E, Vantorre M and Delefortrie G 2012 A prediction method for squat in restricted and unrestricted rectangular fairways *Ocean Eng.* **55** 71-80